Chem

CellPress

Article

Product-Specific Active Site Motifs of Cu for Electrochemical CO_2 Reduction

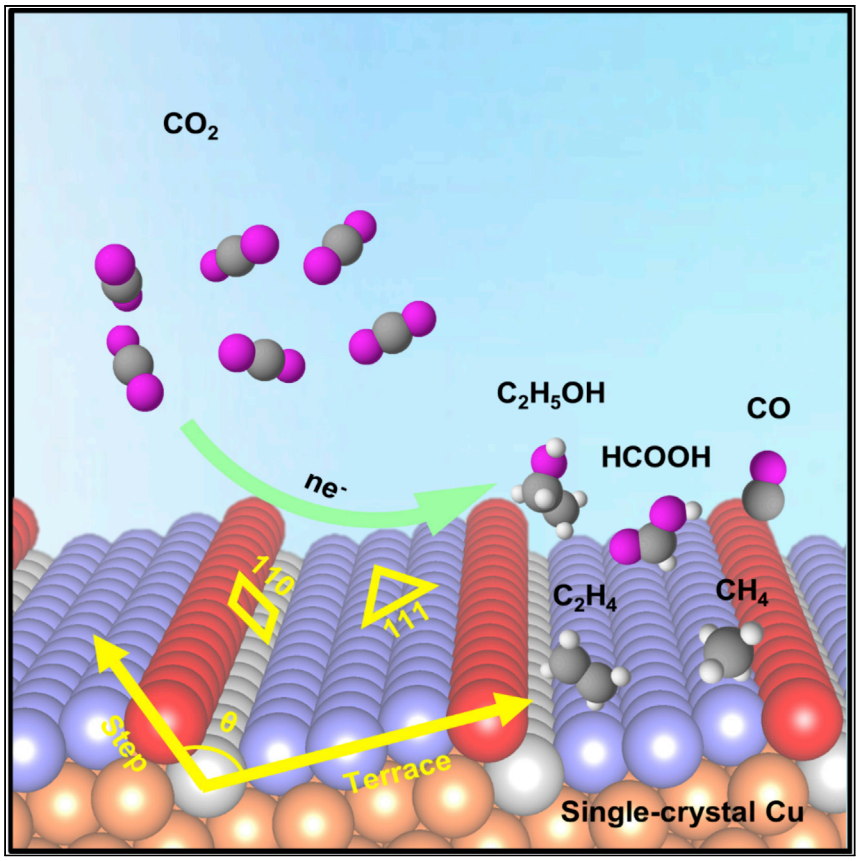

We rationally designed and fabricated nine large-area single-crystal Cu foils with various orientations as electrocatalysts and *operandoly* monitored their surface reconstructions. Quantitative correlations between Cu atomic configurations and the selectivities toward multiple products were established. We extracted three distinct structural descriptors, including crystal facet, atomic coordination number, and step-terrace angle, to reveal the intrinsic structure-function relationships and uniquely identify the specific product-producing sites of Cu for CO_2R.

Chenyuan Zhu, Zhibin Zhang, Lixiang Zhong, ..., Hao Ming Chen, Kaihui Liu, Liming Zhang

lisz@ntu.edu.sg (S.L.)
haomingchen@ntu.edu.tw (H.M.C.)
khliu@pku.edu.cn (K.L.)
zhanglm@fudan.edu.cn (L.Z.)

HIGHLIGHTS

Large-format single-crystal Cu foils were fabricated as electrocatalysts for CO_2R

Operando GIXRD and *ex situ* EBSD monitored the surface reconstruction of Cu

Specific product-producing sites of Cu for CO_2R were identified

Zhu et al., Chem 7, 406–420
February 11, 2021
https://doi.org/10.1016/j.chempr.2020.10.018

CellPress

Chem

Article

Product-Specific Active Site Motifs of Cu for Electrochemical CO_2 Reduction

Chenyuan Zhu,[1,8] Zhibin Zhang,[2,8] Lixiang Zhong,[3,8] Chia-Shuo Hsu,[4,8] Xiaozhi Xu,[5] Yingzhou Li,[6] Siwen Zhao,[1] Shaohua Chen,[1] Jiayi Yu,[1] Shulin Chen,[7] Mei Wu,[7] Peng Gao,[7] Shuzhou Li,[3,*] Hao Ming Chen,[4,*] Kaihui Liu,[2,*] and Liming Zhang[1,9,*]

SUMMARY

Aqueous electrochemical CO_2 reduction (CO_2R) on Cu can generate a variety of valuable fuels, yet challenges remain in the improvement of electrosynthesis pathways for highly selective fuel production. Mechanistically, understanding CO_2R on Cu, particularly identifying the product-specific active sites, is crucial. Herein, we rationally designed and fabricated nine large-area single-crystal Cu foils with various surface orientations as electrocatalysts and identified the voltage- and facet-dependent CO_2R selectivities. *Operando* grazing incidence X-ray diffraction (GIXRD) and electron back-scattered diffraction (EBSD) were applied to track the top-surface reconstructions of Cu, and we correlate the structural evolution with the change of product selectivities. We extracted three distinct structural descriptors, including crystal facet, atomic coordination number, and step-terrace angle, to reveal the intrinsic structure-function relationships and uniquely identify the specific product-producing sites for CO_2R. Our work guides the rational design of Cu-based CO_2R electrocatalysts and, more importantly, establishes a paradigm to understand the structure-function correlation in catalysis.

INTRODUCTION

The direct electrochemical transformation of CO_2 to valuable carbon-based fuels is a promising future technology with the potential to impact large-scale sustainable energy storage and reduce carbon emissions.[1,2] Distinguished from electrochemical water reduction to produce hydrogen, CO_2 reduction (CO_2R) has multiple reaction pathways, leading to a range of reduced carbon fuels, such as C_1 (CO, formate [$HCOO^-$], methane [CH_4], etc.), C_2 (ethylene [C_2H_4], ethanol [C_2H_5OH], etc.), and C_3 (n-propanol [n-C_3H_7OH], etc.).[3,4] To date, significant hurdles regarding the poor selectivity still need to be overcome if electrochemical CO_2R is to become a viable option for storing renewable electricity.[5] To achieve this goal, mechanistically understanding CO_2R, particularly identifying the product-specific active sites, is crucial.[6] Of the reported prevalent electrocatalysts effective for CO_2R, Cu is the only metal catalyst that produces C_{2+} fuels, which are more desirable as feedstocks in the chemical industry, with substantial yields.[3,7–11] Thus, significant attention is devoted to unraveling the factors that determine the activity and selectivity of Cu-based electrocatalysts.

The complexity of CO_2R originates from the multiple electron transfer steps involved and the strong surface structure sensitivity of the process. A number of theoretical works have shown that the activation energies of some key steps in CO_2R, such as

The Bigger Picture

Electrochemical CO_2 reduction (CO_2R) to fuels is a promising route to close the anthropogenic carbon cycle and store renewable energy. Cu is the only metal catalyst that produces C_{2+} fuels, yet challenges remain in the improvement of electrosynthesis pathways for highly selective fuel production. To achieve this, mechanistically understanding CO_2R on Cu, particularly identifying the product-specific active sites, is crucial. We rationally designed and fabricated nine large-area single-crystal Cu foils with various surface orientations as electrocatalysts and monitored their surface reconstructions using *operando* grazing incidence X-ray diffraction (GIXRD) and electron back-scattered diffraction (EBSD). We quantitatively established correlations between the Cu atomic configurations and the selectivities toward multiple products and provide a paradigm to understand the structure-function correlation in catalysis.

*CHO formation and *CO dimerization, etc., highly depend on the surface atomic arrangement.[12–14] Previous analysis demonstrated that the C–C coupling pathway is much favored on Cu(100).[15–17] The catalytic roles of Cu^+ and the positive effect of oxygenated surface species on alcohol production have also been proposed.[18,19] However, the widely used nano-polycrystalline Cu and partially oxidized Cu catalysts generally have very complex atomic geometries[3,18] and pose extreme challenges to directly correlate the atomic structure with the product selectivity. More importantly, the reconstruction of Cu under CO_2R operating conditions is vital to the product generation;[10] however, very few of the previous studies monitored the dynamic change of Cu surface *operandoly*, which precludes a direct relevance between real atomic configuration and catalytic performance.[20] Recently, *in situ* electrochemical scanning tunneling microscopy (EC-STM) demonstrated its remarkable ability in tracking the surface reconstruction of Cu,[21,22] yet it is quite time consuming to obtain a representation of the entire catalyst surface at micro-scale, and severe bubble generation under CO_2R disables effective image collection.[23]

A well-defined surface structure with known composition is essential for the fundamental understanding of parameters that control CO_2R selectivity. Single-crystal Cu is a perfect model system to study structure-function correlations.[24–27] The CO_2R electrocatalysis on single-crystal Cu was first performed by Frese, who observed increasing CH_4 production on Cu(100), Cu(110), and Cu(111) electrodes.[28] Using a galvanostatic method, Hori et al. systematically studied the significant influence of Cu facet on the selectivities of CO_2R products, including CH_4, C_2H_4, CH_3COOH, CH_3CHO, and C_2H_5OH.[29] However, the dynamic surface reconstruction of Cu and its relevance to the change in product selectivities were neglected. In addition, voltage-dependent selectivity was not mentioned in these works, as Hori et al. quantified product generation at a constant current density of 5 mA/cm^2. Recently, $CO_{(2)}R$ on single-crystal Cu with low-index facets—Cu(100) and Cu(111)—has experimentally confirmed that Cu(100) is more active for C–C coupling and Cu(111) is preferable to CH_4 production.[16,17,19,26] The Jaramillo group also explored CO_2R on high-index Cu(751) facet to show the benefit of a kinked surface for oxygenate generation.[26] Despite this progress, the understanding of product-specific active sites on Cu is still limited by voltage-dependent product generation and the *operando* surface reconstruction of Cu. Distinct surface descriptors showing the intrinsic structure-function relationships are still elusive. Additionally, the uniformity of constructed monocrystalline facets and the extreme difficulty to synthesize Cu with exposed high-index facets also pose challenges to understanding CO_2R comprehensively.

Here, we establish quantitative correlations between Cu atomic configurations and the selectivities of multiple products across CO_2R potential window. We rationally designed and fabricated nine large-area single-crystal Cu foils (up to 100 cm^2) as electrocatalysts and monitored their surface reconstructions using *operando* grazing incidence X-ray diffraction (GIXRD) and electron back-scattered diffraction (EBSD), which show the diverse stabilities of different Cu facets. We correlated the structural evolution with the generation of C_1 products (e.g., CO, $HCOO^-$, and CH_4) and C_{2+} products, including C_2H_4 and oxygenate alcohols (e.g., C_2H_5OH and n-C_3H_7OH), at multiple CO_2R potentials. From the perspective of the atomic coordination environment and topological structure, we established three distinct descriptors, including crystal facet, atomic coordination number, and step-terrace angle, to reveal the intrinsic structure-function correlations and uniquely identify the specific product-producing sites of Cu for CO_2R. Overall, our results demonstrate a benchmark system to explicitly link Cu atomic configurations to CO_2R

[1]Department of Chemistry, Fudan University, Shanghai 200438, China

[2]State Key Laboratory for Mesoscopic Physics, Frontiers Science Center for Nano-Optoelectronics, School of Physics, Peking University, Beijing 100871, China

[3]School of Materials Science and Engineering, Nanyang Technological University, Singapore 639798, Singapore

[4]Department of Chemistry, National Taiwan University, Taipei 10617, Taiwan

[5]Guangdong Provincial Key Laboratory of Quantum Engineering and Quantum Materials, School of Physics and Telecommunication Engineering, South China Normal University, Guangzhou 510631, China

[6]Department of Mathematics, Duke University, Durham, NC 27708, USA

[7]Electron Microscopy Laboratory and International Center for Quantum Materials, School of Physics, Peking University, Beijing 100871, China

[8]Those authors contributed equally

[9]Lead Contact

*Correspondence: lisz@ntu.edu.sg (S.L.), haomingchen@ntu.edu.tw (H.M.C.), khliu@pku.edu.cn (K.L.), zhanglm@fudan.edu.cn (L.Z.)

https://doi.org/10.1016/j.chempr.2020.10.018

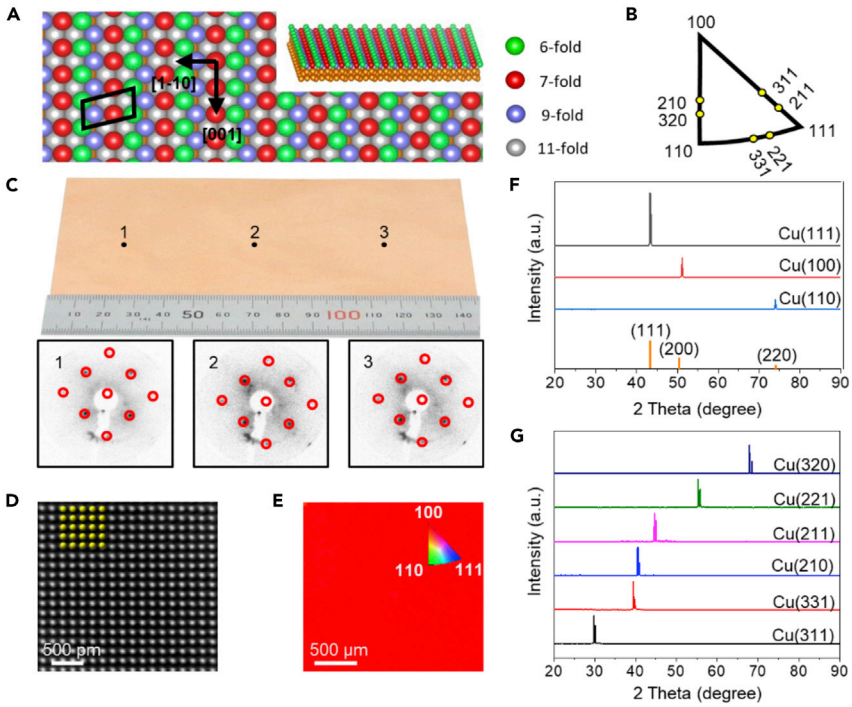

Figure 1. Large-Area Single-Crystal Cu Foils

(A) A schematic illustration of high-index single-crystal Cu(320) facet having surface atoms with distinct coordination environments. The side view is shown as an inset. The coordination numbers of the unsaturated Cu atoms are: six (green), seven (red), nine (blue), and eleven (gray).

(B) An inverse pole figure showing the location of nine monocrystalline Cu facets.

(C) A digital photograph of a large-area single-crystal Cu(100) foil and the representative low-energy electron diffraction (LEED) images sampled at three random locations.

(D and E) Atomically resolved STEM image (D) and large-scale EBSD mapping (E) of Cu(100) foil. Inset of (E) shows the pole figure orientation map.

(F and G) Representative XRD 2 theta-scan of low- (F) and high-index (G) single-crystal Cu foils measured by Cu and Ag targets, respectively.

catalytic performance and provide a paradigm to understand the correlation between atomic configuration and catalysis.

RESULTS AND DISCUSSIONS

Design and Preparation of Large-Area Single-Crystal Cu Foils

According to the Miller indices {hkl}, Cu facets can be classified into low-index facets constituting the small library of {100}, {111}, and {110}, and high-index facets, which constitute terraces, steps, and/or kinks with variable orientations. Using the microfacet notation developed by Somorjai et al. in the 1980's for cubic structures,[30] each high-index facet can be described as a combination of low-index facets with different constitution ratios. For instance, Cu(320) can be described as Cu (S)-[2_2(110)+1_1(100)], indicating that there are two (110) and one (100) unit cells in a (320) unit cell. Thereby, Cu(320) can be visualized as a kinked surface with narrow (110) terraces and a high density of (100) steps (Figure 1A). The angle between the terrace and step is 74.5°. The presence of low-index facets suggests a high degree of site heterogeneity, which can be clearly observed in the inset of Figure 1A, where the kinks in Cu(320) are shown to have atomic sites with six- (green), seven- (red), nine- (blue), and eleven-fold (gray) coordination. To elucidate the structure-function correlation, we rationally designed nine single-crystal Cu facets with distinct

coordination environments and site motifs, including three low-index facets, e.g., Cu(100), Cu(111), and Cu(110), and six high-index facets, e.g., Cu(331), Cu(311), Cu(210), Cu(221), Cu(320), and Cu(211). These high-index facets can be denoted as different combinations of (100), (111), and (110) (Figure S1) and are located on the inverse pole figure as shown in Figure 1B.

Although previous works have fabricated single-crystal Cu electrode/nanoparticles,[17,27,29] the ultra-small single-crystal Cu (< 0.1 cm^2) without a high degree of uniformity and/or the short length scale of nanostructured Cu particles covered with surfactants make it difficult to accurately quantify the atomic structure distributions and to correspondingly elucidate the correlations between the structure configuration and product preference. To address these drawbacks, we prepared large-format single-crystal Cu foils via our most recently developed "seeded abnormal grain growth" technique (see more details in Experimental Procedures).[31] Notably, this strategy can prepare uniform single-crystal electrodes with a super-large geometric area (up to 100 cm^2), thus offering a significant feasibility for the electrochemical device integration, particularly on the *in situ* detection apparatus. Figure 1C shows an optical image of a large-area single-crystal Cu foil with out-of-plane textured along <100> direction. The identical rotation angle in the low energy electron diffraction (LEED) patterns sampled at multiple random positions suggests the absence of the in-plane misorientation on the surface, which can be further corroborated by the atomic-resolved scanning transmission electron microscopy (STEM) image (Figure 1D) and the uniform color contrast of the EBSD mapping (Figure 1E). X-ray diffraction (XRD) was used to track the crystallinity of the bulk Cu foils. As shown in Figures 1F and 1G, XRD symmetric scans establish the single crystallinity nature of fcc Cu foils textured in nine out-of-plane directions, consistent with the LEED patterns, EBSD mapping, and the correlated TEM images summarized in Figures S2–S4. All these results demonstrate that we were able to explicitly control the surface atomic structures of Cu on a decimeter scale.

Single-Crystal Cu Foils for Electrochemical CO_2R

The electrocatalytic activities of single-crystal Cu foils were evaluated by performing electrolysis in a 0.1 M $KHCO_3$ aqueous solution under 1 atm of CO_2 in a two-compartment H-cell. Each Cu surface was tested using chronoamperometry at multiple potentials, and gas and liquid products were quantified using gas chromatography (GC) and nuclear magnetic resonance (NMR) spectroscopy, respectively (see more details in Experimental Procedures; Figures S5–S7). The major products detected were CO, $HCOO^-$, CH_4, C_2H_4, C_2H_5OH, n-C_3H_7OH, and H_2 (produced from the competing proton reduction). Acetate (CH_3COO^-), ethylene glycol ($HOCH_2CH_2OH$), and propionaldhyde (CH_3CH_2CHO) were also observed in intermediate amounts on some single-crystal Cu electrodes, such as Cu(110), Cu(320), and Cu(211). The selectivity, time-dependent current density, and partial current density of each product on both low-and high-index Cu facets were plotted as a function of applied potential, as summarized in Figures S8–S10. As a competitive reaction, proton reduction dominates at both low and high overpotentials, e.g., > −0.7 and < −1.2 V versus RHE (reversible hydrogen electrode), due to the weak CO_2R activity at lower overpotentials and the mass transfer limitation of CO_2 under the large electrochemical polarization, respectively. In the medium potential region, CO_2R kinetically dominates the reaction and is not limited by the supply of CO_2.[3,17] To exclude the influence from mass transport, we focused on the medium potential region to understand CO_2R kinetics in the following study.

To identify product distribution clearly, we grouped CO_2R products as $2e^-$ products (2 mol of e^- are consumed for the generation of product per mol, e.g., CO and

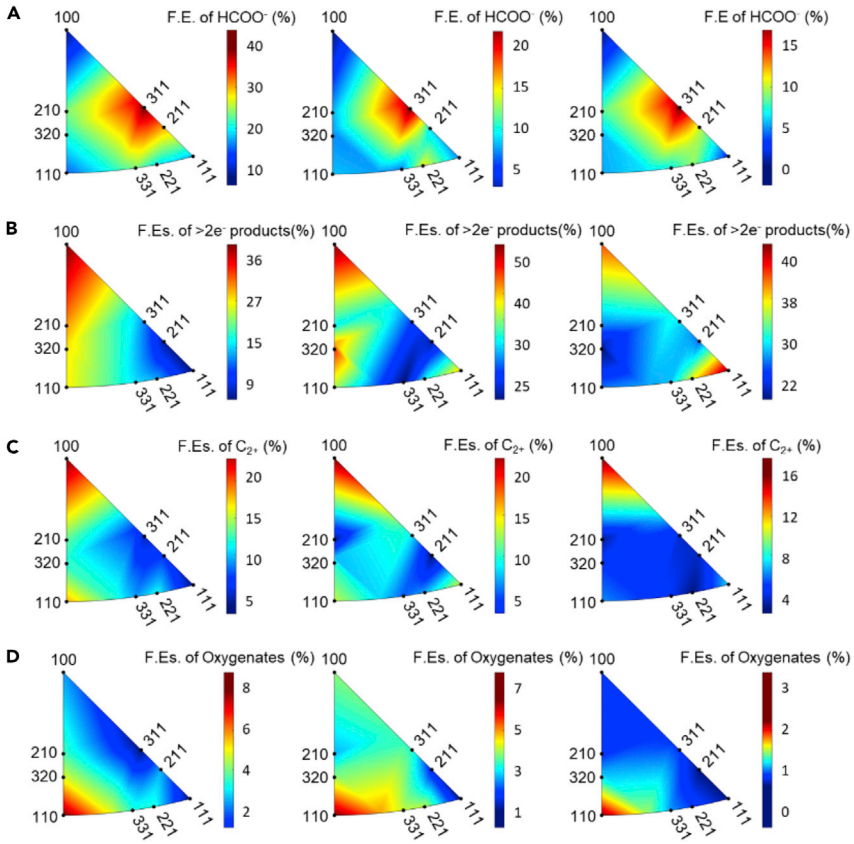

Figure 2. Contour Mapping for the Tendency of Multiple Fuel Generation

(A–D) The F.E(s). of $HCOO^-$ (A), > $2e^-$ products (B), C_{2+} (C), and oxygenates (D) at −0.95 ± 0.01 V (left), −1.05 ± 0.02 V (middle), and −1.15 ± 0.01 V (right) versus RHE on nine single-crystal Cu facets.

$HCOO^-$) and > $2e^-$ products (> 2 mol of e^- are consumed for the generation of product per mol), including CH_4, C_2H_4, and oxygenates (e.g., C_2H_5OH, n-C_3H_7OH, and CH_3COO^-, etc.), and utilized the inverse pole figure to map the product distribution tendency on nine single-crystal orientations under three selected potentials (−0.95, −1.05, and −1.15 V versus RHE). Among CO_2R products, $HCOO^-$ is considered to be a terminal $2e^-$ pathway formed through a different mechanism apart from CO and > $2e^-$ products. As shown in Figure 2A, Cu(211) and Cu(311) are observed to be more preferable for $HCOO^-$ production across the potential window, indicating that Cu-n(111) × (100) is a $HCOO^-$-producing site in CO_2R and is impervious to the potential perturbation. Furthermore, comparing the activities between Cu(311) and (211), we can deduce that the narrower (111) terrace (the smaller angle between terrace and step), the higher the selectivity for $HCOO^-$ production.

To uncover the atomic configuration leading to >$2e^-$ products, we then plotted the total faradic efficiencies (F.Es.) of > $2e^-$ fuels at various potentials on nine Cu facets in Figure 2B, which in contrast to $HCOO^-$, exhibited a tremendous evolution with changing voltage. At −0.95 V versus RHE, the Cu facets containing n(100) × (110) show a higher selectivity toward > $2e^-$ products, consistent with our density functional theory (DFT) calculations showing their lower energy barrier in *CO + H* → *CHO (rate determining step, r.d.s.) for the production of > $2e^-$ fuels (Figure S11).[32] With the negative potential increasing, the preference of > $2e^-$ products on Cu(210)

and Cu(320) is diminishing, and n(111)× (100) dominates > $2e^-$ fuels production at −1.15 V versus RHE. In >$2e^-$ products, CH_4 production also demonstrates an obvious voltage dependence. The line of n(100) × (110) first demonstrated the highest selectivity toward CH_4, which was further surpassed by Cu(110) and Cu(111) with the negative bias increasing (Figure S12). We attributed the initial favorable production of CH_4 on Cu(100) to a higher concentration of adsorbed *CO, as indicated by the higher CO generation rate on Cu(100) before −0.85 V versus RHE (Figure S8).

Distinguished from CH_4 products, the formation of C_{2+} in >$2e^-$ products requires C–C coupling of the adsorbed *CO intermediate,[16] for instance, *CO + *CHO → *CO-CHO[32] has been identified as the r.d.s. We show that, Cu(100) displays a strong preference toward C_{2+} production at different potentials, which can clearly be seen from the contour mappings of the F.Es. of C_{2+} (Figure 2C). Theoretical calculations further corroborate the higher selectivity of C_{2+} on Cu(100) from the lowest formation barrier of *COCHO (Figure S13). As one important component of C_{2+} fuels, C_2H_4 production positively relates with the fraction ratio of Cu(100) lattice (Figure S14), consistent with the previous study of Hori et al.[7] Last but not least, it is useful to compare the selectivity of liquid oxygenate fuels. The contour mapping shown in Figure 2D demonstrates that Cu(110) is most active toward oxygenate production across the potential window, and there also exists a positive correlation between alcohol selectivity and the fraction ratio of (110) in a high-index Cu unit cell (Figure S15).

Overall, it is clear that in CO_2R electrocatalysis, the selectivity toward multiple products is both voltage- and facet-dependent, and our work is the first report, as far as we know, to show the two effects simultaneously. However, it is known that Cu surface undergoes kinetic reconstructions at CO_2R operating conditions.[21,22] To illuminate the product-specific active site motifs, it is desirable to track the time-induced dynamic evolution of Cu surface and illuminate the surface reconstruction.

Operando Dynamic Surface Reconstruction of Cu

We customized a three-electrode liquid cell (Figure S16) for *in situ* GIXRD measurements, in which a kapton polyimide film (DuPont) with a thickness of 0.06 mm served as an X-ray window, and electrolyte thickness was precisely controlled below 1 mm to suppress the interference from liquid electrolyte. The super-large area of single-crystal Cu foils provides a significant feasibility for the electrochemical device integration. Comparing with the *in situ* EC-STM, which is generally used to characterize the local structural evolution of surface, *in situ* GIXRD is capable of showing the average structural evolution in a large area and providing a time-saving quantitative analysis strategy to correlate the real surface atomic configuration with the measured catalytic activity and selectivity toward multiple products. By controlling the incident angle below 0.5°, GIXRD can probe the structural information of Cu surface within a depth of 5 nm. We tracked the evolution of surface orientation on low-index Cu(111), Cu(110), and Cu(100) during chronoamperometric CO_2R electrocatalysis (Figures 3A and S17). Cu(111) and Cu(110) were observed to be quite robust in the time scale of 3 h under a negative potential of −1.15 V versus RHE, indicative of the strong durability of Cu(111) and Cu(110) in CO_2R. For Cu(100), however, we observed a partial structural transformation. A new XRD peak assigned to Cu(111) appeared on Cu(100) in less than 30 min, and stabilized quantificationally at ~15% ($I_{(111)}/I_{(100)}$) after a 3-h electrolysis (Figure 3B). The increased ratio of the (111) unit cell can well explain the increased CH_4 production and decreased C_2H_4 generation at a higher negative bias on Cu(100), as experimentally demonstrated in Figure S8, as well as the second pathway for C_2H_4 production observed previously.[25]

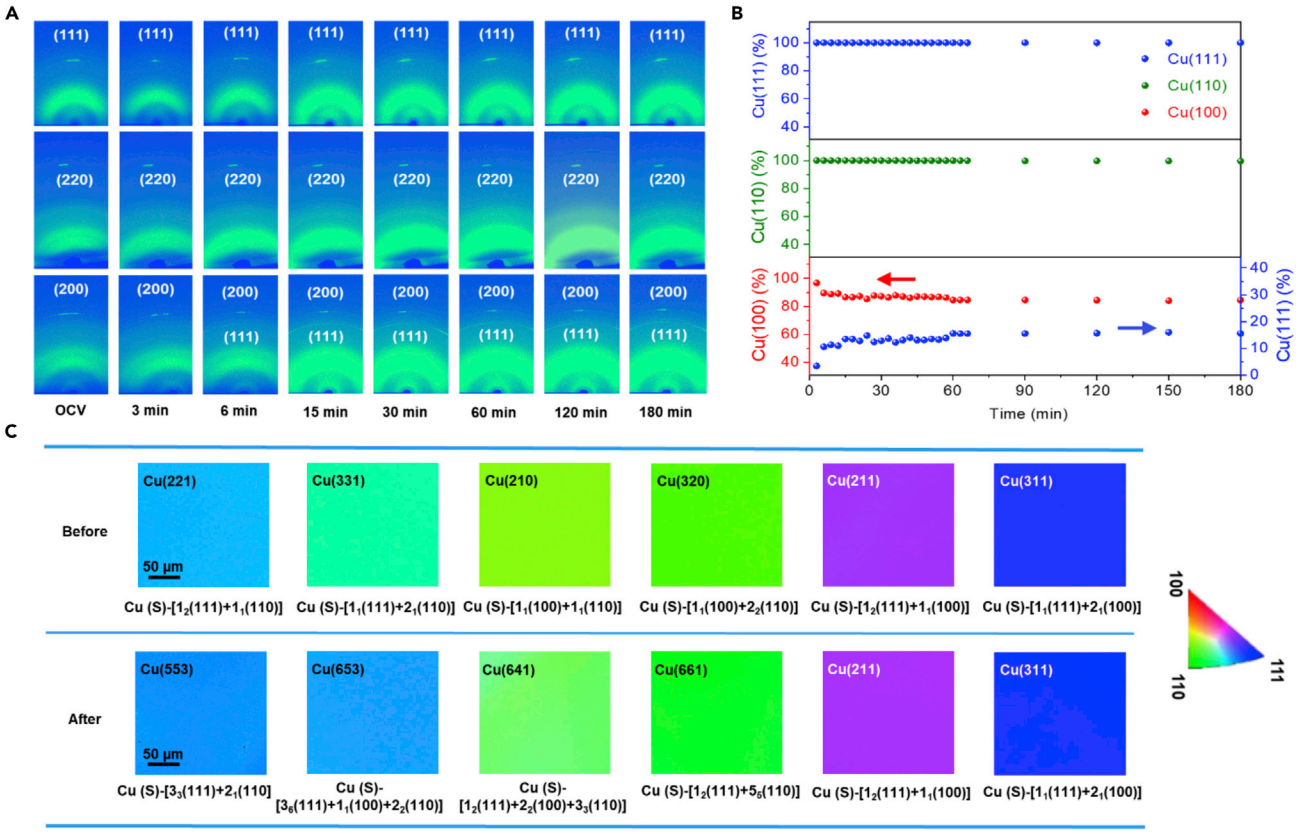

Figure 3. Dynamic Reconstruction of Cu Surface under CO_2R

(A) *Operando* GIXRD images of single-crystal Cu(111), Cu(110), and Cu(100) (from top to bottom) at −1.15 V versus RHE during CO_2R.

(B) Quantitative analysis of Cu(111), Cu(110), and Cu(100) (from top to bottom) surface evolution at −1.15 V versus RHE under CO_2R.

(C) EBSD images (with facet decomposition) of six high-index Cu facets before and after CO_2 electrocatalysis at −1.15V versus RHE.

We further applied EBSD to characterize the surface reconstruction of high-index Cu facets after CO_2R electrolysis at −1.15 V versus RHE *ex situ*, which shows that the fraction ratio of Cu(111) increases on a majority of facets. As listed in Figure 3C, the outer planes of Cu(331), Cu(221), Cu(210), and Cu(320) were transformed to Cu(653), Cu(553), Cu(641) and Cu(661), respectively (see structural models in Figure S18). The increasing ratio of Cu(111) explicitly demonstrates that the closely packed nine-coordinated Cu(111) surface is the most stable facet under CO_2R. This result is consistent with our calculation shown in Figure S19, which confirms the lowest surface energy of Cu(111). The structural evolution can correlate well with the changing of product selectivities under a higher negative bias, for instance, the increased CH_4 and decreased alcohol production on Cu(210), Cu(320), Cu(331), and Cu(221) probably arise from the increased constitution ratio of Cu(111). In stark contrast to these high-index facets undergoing reconstruction, Cu(211) and Cu(311) were unreconstructed after electrocatalysis, consistent with their impervious $HCOO^-$ preference to the potential perturbation.

Product-Specific Active Site Motifs of Cu for CO_2R

Based on the aforementioned results, we aim to extract the product-specific active site motifs of Cu for CO_2R. As the product distribution highly depends on the exact nature of the Cu surface, the structural reconstruction under a higher negative bias should be taken into account. We are aware that the catalysis micro-environment, such as cations in electrolyte,[33] pH values,[34] reduction temperature,[35] etc., also

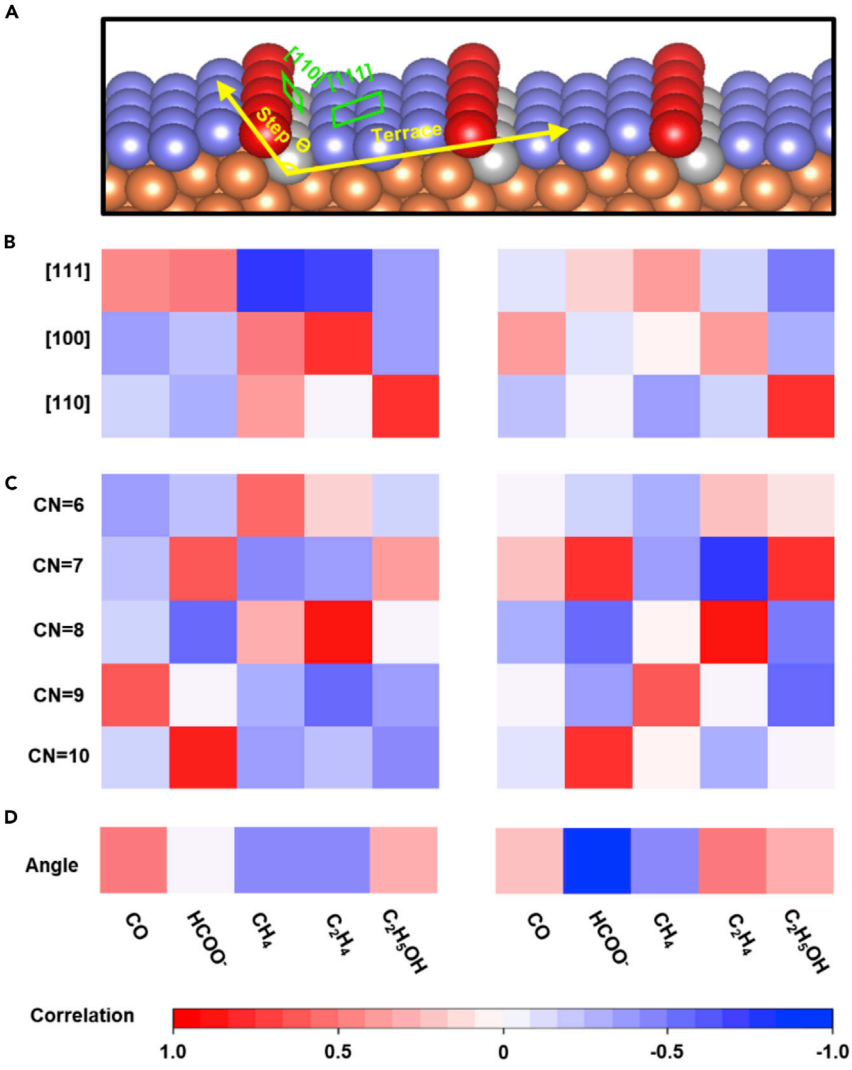

Figure 4. Pearson Correlation Map between Cu Atomic Configurations and Multiple Fuel Generation

(A) Schematic illustration of the atomic coordination environment and topology on an ideal single-crystal Cu surface.

(B–D) Pearson correlation coefficient (from −1 to 1) showing the correlation of lattice facet (B), coordination number of surface atoms (C), and step-terrace angle (D) with the specific product selectivity at −0.95 ± 0.01 V (left column) and −1.15 ± 0.01 V versus RHE (right column), respectively.

influence the product selectivity; however, we aim to reveal the intrinsic structure-function relationships of Cu for CO_2R in this work. Here, we avoid studying the complex reaction pathways of CO_2R and focus instead on descriptors for the structure-dependent product distribution. As depicted in Figure 4, we show the correlations between atomic configurations and various product generation under both −0.95 (left column) and −1.15 V versus RHE (right column). At −1.15 V versus RHE, we utilized the high-index facets Cu(311), Cu(211), Cu(653), Cu(553), Cu(641), and Cu(661) formed after surface reconstruction to extract the surface descriptors. As schematically shown in Figure 4A, we established three distinct descriptors from the perspective of the atomic coordination environment and topological structure, including crystal facet, atomic coordination number, and step-terrace angle, to reveal the

intrinsic structure-function correlations and uniquely identify the specific product-producing sites of Cu for CO_2R. The correlation is calculated as the Pearson correlation coefficient (giving values between −1 and 1) showing the correlation between two variables, in which 1 is a perfect positive linear correlation, 0 is no correlation, and −1 is a perfect negative linear correlation.[36]

As the high-index facet can be described as a combination of low-index facets with different constitution ratios, we first calculated the fraction ratio of Cu(100), Cu(111), and Cu(110), respectively, in all high-index facets before and after surface reconstruction. Figure 4B demonstrates the correlation between the facets and the product-specific selectivities. We first focus on the similarities in correlation under two different potentials. Regardless of the applied voltage, Cu(111), Cu(100), and Cu(110) show an obvious positive correlation with the production of $HCOO^-$, C_2H_4, and C_2H_5OH, respectively. These results suggest that to design a highly active Cu catalyst for $HCOO^-$, C_2H_4, and C_2H_5OH, the Cu surface should have more Cu(111), (100), and (110) lattice, respectively. We also observed that the active facet for CH_4 production is potential dependent. Cu(100) is more active for CH_4 production at a lower negative bias, whereas Cu(111) is more active at a higher negative bias. This transformation may be attributed to the changing interactions between the intermediates and Cu atoms or variable reaction pathways under different potentials. Beyond that, we found Cu(111) negatively correlates with both C_2H_4 and C_2H_5OH across the potential window, Cu(100) inhibits $HCOO^-$ and C_2H_5OH generation, and Cu(110) is unbeneficial for the production of CO.

These experimental results are consistent with our theoretical calculations on three low-index Cu facets (Figures S20–S23). The selectivity between $HCOO^-$ and CO were explored on three low-index Cu facets using DFT calculations. As shown in Figure S20, the maximum energy barrier along the free-energy profiles for $HCOO^-$ and CO generation determines the dominating reaction pathway, and the point deviating from the diagonal line indicates the preferable generation of either CO or $HCOO^-$. These analyses show that in three low-index facets, Cu(111) is apt to produce $HCOO^-$, which is consistent with our experimental observations (Figure S8). In addition, the reaction barrier for *CO-*CHO coupling is only 0.55 eV on Cu(100), whereas it is much higher on Cu(111) (0.75 eV) and Cu(110) (0.81 eV) (Figure S21), confirming the preferable C_2H_4 production on Cu(100). Furthermore, the key step for C_2H_5OH production, reducing *HCCOH to *HCCHOH,[37] is highly favorable in energetics on Cu(110) with an energy drop of 0.66 eV (Figure S22)—much more significant than those on other facets. Interestingly, in contrast to Hori et al.'s results that Cu(111) is the most active facet for CH_4, we only observed a positive correlation between Cu(111) and CH_4 generation under a high negative bias. Instead, at lower negative bias, we observed Cu(100) is preferable toward CH_4 generation. The energy barrier for CH_4 production on three low-index facets was extracted using DFT calculations (Figure S23), which demonstrates a smaller energy barrier on Cu(100) for the key step of CH_4 formation, *CO to *CHO, consistent with our experimental observations (Figure S12).[32]

Next, we correlated the product-specific selectivities with the surface coordination number (CN) of Cu atoms, which is defined as the number of nearest neighboring atoms (Figure 4C). Atoms that have an 8-fold coordination show a strong positive correlation with C_2H_4 generation across the full potential window, consistent with the favorable C_2H_4 production on Cu(100). $HCOO^-$ production was much more preferable on Cu atoms that have a CN of seven and ten under both potentials but was suppressed on the atoms having a CN of eight. Instead, C_2H_5OH production could

be promoted on a more "open" surface, which consist of more Cu atoms having a smaller CN, such as six and seven. In addition, voltage-dependent CH_4 production could also be observed, which displayed a higher activity on atoms that have a CN of eight and nine at a lower and higher negative bias, respectively.

In addition to the atomic coordination environment, we also extracted the correlation between the product tendency and step-terrace angle, from the perspective of topological structure (Figure 4D). Across the full potential window, a larger step-terrace angle is beneficial for C_2H_5OH generation, on the contrary, CH_4 production is preferable on the Cu surface having a smaller step-terrace angle. These results demonstrate that both the atomic coordination environment and topological structure are capable of influencing the product distribution of CO_2R on the Cu catalyst.

Conclusion

In conclusion, we unambiguously demonstrated a correlation between Cu atomic configurations and the selectivities toward multiple fuels. We rationally designed and fabricated large-area single-crystal Cu foils with various surface orientations, tracked the dynamic top-surface reconstruction of Cu facets under CO_2R, and revealed the product-specific active sites of Cu toward CO_2R by correlating the atomic structures with the product selectivities. Our work demonstrates a benchmark system for CO_2R electrocatalysis and provides an important mechanistic insight that could further guide the rational design and optimization of Cu-based CO_2R catalysts. This analysis method can be straightforwardly extended to other single-crystal electrodes, as well as other chemistries, to unravel the active site motifs of catalysts.

EXPERIMENTAL PROCEDURES

Resource Availability

Lead Contact

Further information and requests for resources and reagents should be directed to the Lead Contact, Liming Zhang (zhanglm@fudan.edu.cn).

Materials Availability

The materials generated in this study will be made available on request.

Data and Code Availability

All of the data are available from the corresponding author upon reasonable request.

Seeded Growth of Single-Crystal Cu Foils

We followed our most recently designed "seeded abnormal grain growth" technique to successfully fabricate the large-area single-crystal Cu foils with nine low- and high-index facets from commercially available polycrystalline Cu foils.[31] Typically, we first pre-oxidized the polycrystalline Cu foil in air to generate a large grain seed with a low- or high-index facet and further annealed it in a reducing atmosphere to enable the abnormal grain growth of the seed, which subsequently turns the whole foil into a single crystal. The detailed preparation procedure is as follows: we first loaded the Cu foil (25 μm-thick, 99.8%, Sichuan Oriental Stars Trading Co. Ltd., #Cu-1031) into a chemical vapor deposition (CVD) furnace (Tianjin Kaiheng Co. Ltd.) using a quartz substrate. Through mild heating, the Cu foil was oxidized at 150°C–650°C in air for 1–4 h. After the pre-oxidation, the system was heated to 1,020°C in 1 h with 800 sccm Ar and 50 sccm H_2, then the Cu foil was annealed at 1,020°C for 3–10 h under the same atmosphere, and finally, the system was naturally

cooled down to room temperature to obtain large-scale single-crystal Cu foils (the system was kept at atmospheric pressure throughout the annealing process). By repeating the typical annealing procedure, nine kinds of single-crystal Cu foils can be produced.

Physical Characterization

LEED measurements were performed using Omicron LEED system in ultra-high vacuum with base pressure below 3×10^{-7} Pa. STEM experiments were carried out on FEI Titan Themis G^2 300 operated at 300 keV. EBSD characterization was performed using PHI 710 Scanning Auger Nanoprobe. The phase purity of each sample was examined by XRD 2θ-scan measurements using a Bruker D8 Advanced system with Cu (Cu Kα radiation, λ = 1.54 Å) and Ag (Ag Kα radiation, λ = 0.56 Å) targets for low- and high-index facet characterization, respectively.

Electrochemical CO_2 Reduction

Pretreatment of Cu Single-Crystal Electrodes

The single-crystal Cu foils were first physically polished with alumina slurries (0.3 μm, CH instrument) to mirror-like finishes and were then electropolished in a H_3PO_4 aqueous electrolyte at a constant potential of 1.5 V versus Ag/AgCl for 90 s.

CO_2R Electrochemical Measurements

The electrocatalytic characterizations were carried out in a customized H-cell, which has two compartments separated by an anion exchange membrane (Fumatech company, Fumasep FAA-3-PK130). Each compartment contained 6 mL of electrolyte (0.1 M $KHCO_3$ aqueous solution, pH 6.8), and the compartment holding the working electrode was sealed to measure gaseous products. The electrolyte was purged with CO_2 at a constant flow rate of 20 sccm for 20 min before and during each measurement while stirring. A platinum wire and a Ag/AgCl (CHI, 3M KCl) were used as counter and reference electrodes, respectively. The potentials measured were converted to RHE scale by V (versus RHE) = V (versus Ag/AgCl, 3M KCl) + 0.210 V + 0.0591 × pH. The solution resistance was compensated for 85% by the potentiostat and the rest 15% was post-corrected.

All the electrochemical measurements were explored using a Biologic-SP300 potentiostat. Before electrolysis, linear sweep voltammetry (at a scan rate of 50 mV/s) was performed and then a set potential was applied for chronoamperometry (CA). During the constant potential electrolysis (1 h), the gas products were quantified using a GC (Agilent 7890B; column HP-PLOT). Samples for GC were collected at 20-min intervals, and the separated gas products were analyzed by both a thermal conductivity detector (for H_2) and a flame ionization detector (for CO and hydrocarbons). Liquid products were analyzed afterward by 500 MHz NMR (AVANCE III HD) using dimethyl sulfoxide and phenol as an internal standard. Solvent presaturation technique was implemented to suppress the water peak. Faradic efficiencies were calculated from the amount of charge passed to produce each product, divided by the total charge passed at a specific time (gas) or during the overall run (liquid).

Calculation of the faradic efficiency of gas products:

$$F.E.(gas) = \frac{F_{flow} \times (C_{gas}/V_m) \times n \times F}{I_{total} \times 60} \times 100$$

Calculation of the faradic efficiency of liquid products:

$$F.E.(liquid) = \frac{C_{liquid} \times V \times n \times F}{Q_{total}} \times 100$$

F.E. (*gas*): faradic efficiency of gas product, %

F.E. (*iquid*): faradic efficiency of liquid product, %

F_{flow}: flow rate of CO_2, mL min^{-1}

C_{gas}: volume ratio of gas product, determined by on-line GC

V_m: the molar volume of an ideal gas at 1 atmosphere of pressure (molar volume at normal temperature and pressure is 0.0245 mL), mL mol^{-1}

C_{liquid}: concentration of liquid product after 1 h of electrolysis, determined by NMR, mol L^{-1}

V: volume of the electrolyte in the working cell, L

I_{total}: steady-state cell current

Q_{total}: total charge in 1 h of bulk electrolysis, C

n: number of transferred electrons for certain product

F: Faradic constant, 96,485 C mol^{-1}

Operando GIXRD Measurement

The GIXRD of the Cu foils were performed at the 12B beamline of Japan, in which the ring was operated at energy 8 GeV with a typical current of 100 mA. Two pairs of slits and one collimator were set up in experimental hutch to provide a collimated beam with a beam size of 300 μm at the sample position. An incident angle of 0.5° was employed in the present study, in which the X-ray irradiation can pass through 5 nm upon surface of sample. The geometry allows us to significantly enhance the X-ray scattering intensity from the surface of Cu foils. The grazing angle was optimized to probe the interior of the sample surface and to achieve the best S/N ratio for maximizing the scattering signal from the electrode surface. In the present study, the wavelength of the incident X-ray was 0.6909 Å (16 keV), delivered from the 5 T Superconducting Wavelength Shifter and a Si (111) triangular crystal monochromator, which allowed an optimized condition for distinguishing scattering rings to be achieved. The diffraction pattern was collected with a MX225-HE Rayonix CCD detector that was located ~195 mm behind the sample, while the total pixel was 3,072 × 3,072 and the pixel size of image was 73 μm with a typical exposure duration of 1 s. To achieve a correct condition, the diffraction angles were calibrated according to Bragg positions of CeO_2 (SRM 674b) standards in desired geometry, and then a program of GSAS II was employed to obtain the corresponding one-dimensional powder diffraction profile with cake-type integration. In terms of the liquid cell, a kapton polyimide film (DuPont) with a thickness of 0.06 mm served as X-ray window, and the thickness of electrolyte was precisely controlled below 1 mm to suppress the interference from liquid electrolyte.

Computational Methods

All the calculations were performed using DFT as implemented in the Vienna *ab initio* simulation package (VASP).[38] The ion-electron interactions were treated with the projected augmented wave (PAW) pseudopotentials,[39] and the plane-wave basis set was cut off at 400 eV. The general gradient approximation (GGA) parameterized by Perdew, Burke, and Ernzerhof (PBE) was adopted to describe the exchange-correlation functional in structural relaxations.[40] All structures were fully relaxed by a conjugate gradient method until the residual force component was less than 0.02 eV/Å, and the convergence criterion of total energy in the self-consistent field method was set to 10^{-5} eV. The optimized lattice constant of Cu is 3.627 Å. The slab model was used to simulate Cu surfaces, where the thickness of the vacuum was larger than 15 Å to make sure that there was no superficial interaction between different layers. The size of the super cells was larger than 10 Å, and the k-point grids (~0.2 $Å^{-1}$) used for the Brillouin-zone integration were sampled by the Monkhorst-Pack scheme.[41] Larger cells or denser k-points yielded the same results in our test calculations. The climbing-image nudged elastic band method was used to locate the transition state and determine the activation energy.[42] The Gibbs free energies (ΔG) of different intermediates were calculated to characterize the CO_2R performance on Cu facets. Chemisorption energies of the reaction intermediates were calculated by:

$$\Delta E_{adsorbate} = E_{total} - E_{substrate} - E_{adsorbate},$$

where E_{total} and $E_{substrate}$ are the DFT energies for the system with and without adsorbate, respectively, and $E_{adsorbate}$ is calculated relative to CO_2, H_2O, and H_2. The corresponding free energy of chemisorption was then calculated by correcting for the zero-point vibrational energy E_{ZPE}, entropy TS, and solvation energy E_{sol}.

$$\Delta G_{adsorbate} = \Delta E_{adsorbate} + \Delta (E_{ZPE} - TS + E_{sol}),$$

where $\Delta G_{adsorbate}$ was used to construct the free-energy profiles. The solvation effects were simulated by using the Poisson-Boltzmann continuum-solvation model in the VASPsol code.[43]

SUPPLEMENTAL INFORMATION

Supplemental Information can be found online at https://doi.org/10.1016/j.chempr.2020.10.018.

ACKNOWLEDGMENTS

This research was supported by the National Natural Science Foundation of China (grants 21872039, 51991340, and 51991342), Science and Technology Commission of Shanghai Municipality (grant 18JC1411700), National Key Research and Development Program of China (2016YFA0300903 and 2016YFA0300804), Beijing Natural Science Foundation (JQ19004), Beijing Excellent Talents Training Support (2017000026833ZK11), Beijing Municipal Science & Technology Commission (Z191100007219005), Beijing Graphene Innovation Program (Z181100004818003), and the Key Research and Development Program of Guangdong Province (2020B010189001, 2019B010931001, and 2018B030327001). We sincerely thank Dr. Bing Deng, Prof. Hailin Peng, and Prof. Zhongfan Liu for providing some low-index single-crystal Cu electrodes when initiating the work.

AUTHOR CONTRIBUTIONS

L.Z. and C.Z. designed and conceived the experiment. C.Z., S.C., S.Z., and J.Y. fabricated the electrodes and performed the electrochemical characterization and data

analysis. B.Z. and K.L. carried out the synthesis of single-crystal Cu foils and LEED characterization. C.S.H. and H.M.C. performed the *operando* GIXRD measurements. L.Z. and S.L. worked on the DFT calculations. S.C., M.W., and P.G. carried out the TEM characterization. Y.L. helped with the modeling and data fitting. All authors discussed the results and participated in writing the manuscript.

DECLARATION OF INTERESTS

The authors declare no competing interests.

Received: June 23, 2020
Revised: July 24, 2020
Accepted: October 17, 2020
Published: November 11, 2020

REFERENCES

1. Seh, Z.W., Kibsgaard, J., Dickens, C.F., Chorkendorff, I.B., Nørskov, J.K., and Jaramillo, T.F. (2017). Combining theory and experiment in electrocatalysis: insights into materials design. Science *355*, eaad4998.

2. Ross, M.B., De Luna, P.D., Li, Y.F., Dinh, C.T., Kim, D., Yang, P., and Sargent, E.H. (2019). Designing materials for electrochemical carbon dioxide recycling. Nat. Catal. *2*, 648–658.

3. Kuhl, K.P., Cave, E.R., Abram, D.N., and Jaramillo, T.F. (2012). New insights into the electrochemical reduction of carbon dioxide on metallic copper surfaces. Energy Environ. Sci. *5*, 7050–7059.

4. Gao, D., Arán-Ais, R.M., Jeon, H.S., and Roldan Cuenya, B. (2019). Rational catalyst and electrolyte design for CO_2 electroreduction towards multicarbon products. Nat. Catal. *2*, 198–210.

5. Bushuyev, O.S., De Luna, P.D., Dinh, C.T., Tao, L., Saur, G., van de Lagemaat, J., Kelley, S.O., and Sargent, E.H. (2018). What should we make with CO_2 and how can we make it? Joule *2*, 825–832.

6. Birdja, Y.Y., Pérez-Gallent, E., Figueiredo, M.C., Göttle, A.J., Calle-Vallejo, F., and Koper, M.T.M. (2019). Advances and challenges in understanding the electrocatalytic conversion of carbon dioxide to fuels. Nat. Energy *4*, 732–745.

7. Kuhl, K.P., Hatsukade, T., Cave, E.R., Abram, D.N., Kibsgaard, J., and Jaramillo, T.F. (2014). Electrocatalytic conversion of carbon dioxide to methane and methanol on transition metal surfaces. J. Am. Chem. Soc. *136*, 14107–14113.

8. Kortlever, R., Shen, J., Schouten, K.J.P., Calle-Vallejo, F., and Koper, M.T.M. (2015). Catalysts and reaction pathways for the electrochemical reduction of carbon dioxide. J. Phys. Chem. Lett. *6*, 4073–4082.

9. Hori, Y., Takahashi, I., Koga, O., and Hoshi, N. (2003). Electrochemical reduction of carbon dioxide at various series of copper single crystal electrodes. J. Mol. Catal. A Chem. *199*, 39–47.

10. Kim, D., Kley, C.S., Li, Y., and Yang, P. (2017). Copper nanoparticle ensembles for selective electroreduction of CO_2 to C_2-C_3 products. Proc. Natl. Acad. Sci. USA *114*, 10560–10565.

11. Zhuang, T.T., Pang, Y., Liang, Z.-Q., Wang, Z., Li, Y., Tan, C.-S., Li, J., Dinh, C.T., De Luna, P.D., Hsieh, P., et al. (2018). Copper nanocavities confine intermediates for efficient electrosynthesis of C_3 alcohol fuels from carbon monoxide. Nat. Catal. *1*, 946–951.

12. Peterson, A.A., Abild-Pedersen, F., Studt, F., Rossmeisl, J., and Nørskov, J.K. (2010). How copper catalyzes the electroreduction of carbon dioxide into hydrocarbon fuels. Energy Environ. Sci. *3*, 1311–1315.

13. Garza, A.J., Bell, A.T., and Head-Gordon, M. (2018). Mechanism of CO_2 reduction at copper surfaces: pathways to C_2 products. ACS Catal. *8*, 1490–1499.

14. Montoya, J.H., Shi, C., Chan, K., and Nørskov, J.K. (2015). Theoretical insights into a CO dimerization mechanism in CO_2 electroreduction. J. Phys. Chem. Lett. *6*, 2032–2037.

15. Wang, Y., Wang, Z., Dinh, C.-T., Li, J., Ozden, A., Golam Kibria, M.G., Seifitokaldani, A., Tan, C., Gabardo, C.M., Luo, M., et al. (2020). Catalyst synthesis under CO_2 electroreduction favours faceting and promotes renewable fuels electrosynthesis. Nat. Catal. *3*, 98–106.

16. Loiudice, A., Lobaccaro, P., Kamali, E.A., Thao, T., Huang, B.-H., Ager, J.W., and Buonsanti, R. (2016). Tailoring copper nanocrystals towards C_2 products in electrochemical CO_2 reduction. Angew. Chem. Int. Ed. *55*, 5789–5792.

17. Huang, Y., Handoko, A.D., Hirunsit, P., and Yeo, B.S. (2017). Electrochemical reduction of CO_2 using copper single-crystal surfaces: effects of CO* coverage on the selective formation of ethylene. ACS Catal. *7*, 1749–1756.

18. Li, C.W., and Kanan, M.W. (2012). CO_2 reduction at low overpotential on Cu electrodes resulting from the reduction of thick Cu_2O films. J. Am. Chem. Soc. *134*, 7231–7234.

19. Jiang, K., Sandberg, R.B., Akey, A.J., Liu, X., Bell, D.C., Nørskov, J.K., Chan, K., and Wang, H. (2018). Metal ion cycling of Cu foil for selective C-C coupling in electrochemical CO_2 reduction. Nat. Catal. *1*, 111–119.

20. Handoko, A.D., Wei, F., Jenndy, Yeo, B.S., and Seh, Z.W. (2018). Understanding heterogeneous electrocatalytic carbon dioxide reduction through operando techniques. Nat. Catal. *1*, 922–934.

21. Kim, Y.G., Baricuatro, J.H., Javier, A., Gregoire, J.M., and Soriaga, M.P. (2014). The evolution of the polycrystalline copper surface, first to Cu(111) and then to Cu(100), at a fixed CO_2RR potential: a study by *operando* EC-STM. Langmuir *30*, 15053–15056.

22. Kim, Y.G., Javier, A., Baricuatro, J.H., Torelli, D., Cummins, K.D., Tsang, C.F., Hemminger, J.C., and Soriaga, M.P. (2016). Surface reconstruction of pure-Cu single-crystal electrodes under CO-reduction potentials in alkaline solutions: a study by seriatim ECSTM-DEMS. J. Electroanal. Chem. *780*, 290–295.

23. Pfisterer, J.H.K., Liang, Y., Schneider, O., and Bandarenka, A.S. (2017). Direct instrumental identification of catalytically active surface sites. Nature *549*, 74–77.

24. Bagger, A., Ju, W., Varela, A.S., Strasser, P., and Rossmeisl, J. (2019). Electrochemical CO_2 reduction: classifying Cu facets. ACS Catal. *9*, 7894–7899.

25. Schouten, K.J., Qin, Z., Pérez Gallent, E., and Koper, M.T.M. (2012). Two pathways for the formation of ethylene in CO reduction on single-crystal copper electrodes. J. Am. Chem. Soc. *134*, 9864–9867.

26. Hahn, C., Hatsukade, T., Kim, Y.G., Vailionis, A., Baricuatro, J.H., Higgins, D.C., Nitopi, S.A., Soriaga, M.P., and Jaramillo, T.F. (2017). Engineering Cu surfaces for the electrocatalytic conversion of CO_2: controlling selectivity toward oxygenates and hydrocarbons. Proc. Natl. Acad. Sci. USA *114*, 5918–5923.

27. Suen, N., Kong, Z., Hsu, C., Chen, H., Tung, C., Lu, Y., Dong, C., Shen, C., Chung, J., and Chen, H.M. (2019). Morphology manipulation of copper nanocrystals and product selectivity in the electrocatalytic reduction of carbon dioxide. ACS Catal. *9*, 5217–5222.

28. Frese, K.W., Jr. (1993). In Electrochemical and Electrocatalytic Reactions of Carbon Dioxide, B.P. Sullivan, K. Krist, and H.E. Guard, eds. (Elsevier).

29. Hori, Y., Takahashi, I., Koga, O., and Hoshi, N. (2002). Selective formation of C_2 compounds from electrochemical reduction of CO_2 at a series of copper single crystal electrodes. J. Phys. Chem. B *106*, 15–17.

30. Van Hove, M.A., and Somorjai, G.A. (1980). A new microfacet notation for high-Miller-index surfaces of cubic materials with terrace, step and kink structures. Surf. Sci. *92*, 489–518.

31. Wu, M., Zhang, Z., Xu, X., Zhang, Z., Duan, Y., Dong, J., Qiao, R., You, S., Wang, L., Qi, J., et al. (2020). Seeded growth of large single-crystal copper foils with high-index facets. Nature *581*, 406–410.

32. Todorova, T.K., Schreiber, M.W., and Fontecave, M. (2020). Mechanistic understanding of CO_2 reduction reaction (CO_2RR) toward multicarbon products by heterogeneous copper-based catalysts. ACS Catal. *10*, 1754–1768.

33. Resasco, J., Lum, Y., Clark, E., Zeledon, J.Z., and Bell, A.T. (2018). Effects of anion identity and concentration on electrochemical reduction of CO_2. ChemElectroChem *5*, 1064–1072.

34. Lim, C.F.C., Harrington, D.A., and Marshall, A.T. (2017). Effects of mass transfer on the electrocatalytic CO_2 reduction on Cu. Electrochim. Acta *238*, 56–63.

35. Ahn, S.T., Abu-Baker, I., and Palmore, G.T.R. (2017). Electroreduction of CO_2 on polycrystalline copper: effect of temperature on product selectivity. Catal. Today *288*, 24–29.

36. Pearson, K. (1920). Notes on the history of correlation. Biometrika *13*, 25–45.

37. Li, Y.C., Wang, Z., Yuan, T., Nam, D.-H., Luo, M., Wicks, J., Chen, B., Li, J., Li, F., de Arquer, F.P.G., et al. (2019). Binding Site diversity promotes CO_2 electroreduction to ethanol. J. Am. Chem. Soc. *141*, 8584–8591.

38. Kresse, G., and Furthmüller, J. (1996). Efficient iterative schemes for *ab initio* total-energy calculations using a plane-wave basis set. Phys. Rev. B Condens. Matter *54*, 11169–11186.

39. Blöchl, P.E. (1994). Projector augmented-wave method. Phys. Rev. B Condens. Matter *50*, 17953–17979.

40. Perdew, J.P., Burke, K., and Ernzerhof, M. (1996). Generalized gradient approximation made simple. Phys. Rev. Lett. *77*, 3865–3868.

41. Monkhorst, H.J., and Pack, J.D. (1976). Special points for Brillouin-zone integrations. Phys. Rev. B *13*, 5188–5192.

42. Henkelman, G., Uberuaga, B.P., and Jónsson, H. (2000). A climbing image nudged elastic band method for finding saddle points and minimum energy paths. J. Chem. Phys. *113*, 9901–9904.

43. Mathew, K., Sundararaman, R., Letchworth-Weaver, K., Arias, T.A., and Hennig, R.G. (2014). Implicit solvation model for density-functional study of nanocrystal surfaces and reaction pathways. J. Chem. Phys. *140*, 084106.